Accumulation of Elastic Strain toward Crustal Fracture in Magnetized Neutron Stars

Yasufumi Kojima
Department of Physics, Hiroshima University, Higashi-Hiroshima, 739-8526, Japan; ykojima-phys@hiroshima-u.ac.jp

Abstract

This study investigates elastic deformation driven by the Hall drift in a magnetized neutron-star crust. Although the dynamic equilibrium initially holds without elastic displacement, the magnetic-field evolution changes the Lorentz force over a secular timescale, which inevitably causes the elastic deformation to settle in a new force balance. Accordingly, elastic energy is accumulated, and the crust is eventually fractured beyond a particular threshold. We assume that the magnetic field is axially symmetric, and we explicitly calculate the breakup time, maximum elastic energy stored in the crust, and spatial shear–stress distribution. For the barotropic equilibrium of a poloidal dipole field expelled from the interior core without a toroidal field, the breakup time corresponds to a few years for the magnetars with a magnetic-field strength of $\sim 10^{15}$ G; however, it exceeds 1 Myr for normal radio pulsars. The elastic energy stored in the crust before the fracture ranges from 10^{41} to 10^{45} erg, depending on the spatial-energy distribution. Generally, a large amount of energy is deposited in a deep crust. The energy released at a fracture is typically $\sim 10^{41}$ erg when the rearrangement of elastic displacements occurs only in the fragile shallow crust. The amount of energy is comparable to the outburst energy on the magnetars.

Unified Astronomy Thesaurus concepts: Neutron stars (1108); Magnetars (992); Compact objects (288); High energy astrophysics (739); Magnetic fields (994); Soft gamma-ray repeaters (1471)

1. Introduction

Neutron-star crust is considered a key aspect for understanding several astrophysical phenomena. The solid layer near the stellar surface can support nonspherical deformations, called mountains, with a height of less than 1 cm. Such asymmetries on a spinning star cause the continuous emission of gravitational waves. Therefore, the calculation of the maximum size of these mountains is the key to the detection of gravitational waves and has been discussed in several theoretical studies (Ushomirsky et al. 2000; Payne & Melatos 2004; Haskell et al. 2006; Gittins et al. 2021). Gravitational-wave observation provides valuable information (Abbott et al. 2021a, 2021b, 2022, for recent upper limit); thus, by continuously improving the sensitivity of the LIGO-Virgo-KAGRA detectors, the physics relevant to the phenomenon may be explored.

Pulsar glitches are sudden spin-up events that are observed in radio pulsars (Espinoza et al. 2011; Basu et al. 2022, for glitch catalog). Similar spin-up and peculiar spin-down events are observed in anomalous X-ray pulsars (Dib et al. 2008; Kaspi & Beloborodov 2017). A sudden spin-up in a radio pulsar is produced by the transfer of angular momentum from the superfluid components of the core to the normal crust (Anderson & Itoh 1975; Alpar et al. 1984). Crust quakes were also discussed in other models (Franco et al. 2000; Giliberti et al. 2020; Rencoret et al. 2021, for recent studies). The elastic deformation is caused by a decrease in centrifugal force, owing to a secular spin-down, and the crust eventually fractures when the strain exceeds a critical threshold. However, this simple model does not explain the observation; the loading of the solid crust between glitches is too insignificant to trigger a quake.

Giant flares in magnetars are rare, albeit highly energetic. They are typically $\sim 10^{44}$–10^{46} erg released within a second (Turolla et al. 2015; Kaspi & Beloborodov 2017; Esposito et al. 2021, for a review). Quasi-periodic oscillations (QPOs) with some discrete frequencies in the range of 20–2 kHz were observed in the tails of these flares. Per the order-of-magnitude estimate, these frequencies correspond to the torsional shear or Alfvén modes with magnetic-field strength $\sim 10^{15}$ G. Outbursts, which are less energetic, are also observed in magnetars. These activities are considered to be powered by internal strong magnetic fields of $\sim 10^{15}$ G. The crustal fracture of the magnetar is proposed as a model for fast radio bursts (FRBs; Suvorov & Kokkotas 2019; Wadiasingh & Chirenti 2020), and it may be supported by QPOs (Li et al. 2022) in the radio burst from SGR J1935+2154 in the galaxy (Mereghetti et al. 2020; CHIME/FRB Collaboration et al. 2020; Bochenek et al. 2020). Most FRBs are located at a cosmological distance, and further observation sheds light on whether FRBs originate from magnetars or a subclass. A recent observation of the magnetar SGR 1830-0645 revealed pulse-peak migration during the first 37 days of outburst decay (Younes et al. 2022). This provides important information concerning the crust motion coupled with the exterior magnetosphere.

Most theoretical studies have been focused on the crustal-deformation limit. Elastic stresses gradually accumulate until a particular threshold. Beyond this threshold, the elastic behavior of the lattice abruptly ceases, and the transition is exhibited as a starquake or burst. An evolutionary calculation of the deformation is necessary to understand the related astrophysical phenomena.

In this study, we consider the crust in a magnetized neutron star. The static magneto-elastic force balance was studied for various magnetic-field configurations (Kojima et al. 2021a, 2022). A variety of magneto-elastic equilibria was demonstrated, and is considerably different from the barotropic equilibrium without a solid crust. Herein, we explore the accumulation of shear stress induced by the Hall evolution, which is an important process in the strong field-strength regime. Suppose that the magnetohydrodynamical (MHD) equilibrium in the crust holds at a particular time without the elastic force. The equilibrium is not that for electrons

(Gourgouliatos et al. 2013; Gourgouliatos & Cumming 2014); thus, the magnetic field tends to the Hall equilibrium in a secular timescale. According to the magnetic-field evolution, the Lorentz force also changes. The deviation is assumed to be balanced with the elastic force. Thus, the shear stress in the crust gradually accumulates and reaches a critical limit. We cannot follow the post-failure evolution because some uncertainties are involved in the discontinuous transition. Therefore, our study provides the recurrent time and magnitude of the bursts.

The models and equations used in the study are discussed in Section 2. For MHD equilibrium in a barotropic star, the evolution of the magnetic field is driven by a spatial gradient of electron density. In Section 3, the critical configuration at the elastic limit is evaluated, and the accumulating elastic energy is calculated. In Section 4, we also consider nonbarotropic effects using simple models. The nonbarotropicity results in another driving process of the magnetic-field evolution, and conse-quently elastic deformation. The numerical results of these models are given. Finally, our conclusions are presented in Section 5.

2. Formulation and Model

2.1. Magnetic Equilibrium

We consider the dynamical force balance between pressure, gravity, and the Lorentz force. The MHD equilibrium is described as follows:

$$-\frac{1}{\rho}\boldsymbol{\nabla}P - \boldsymbol{\nabla}\Phi_{\mathrm{g}} + \frac{1}{c\rho}\boldsymbol{j} \times \boldsymbol{B} = 0, \tag{1}$$

where Φ_{g} is the gravitational potential including the centrifugal terms. The third term has a magnitude $\sim 10^{-7}(B/10^{14}\mathrm{G})^2$ times smaller than those of the first and second terms. Deviation owing to the Lorentz force is small enough to be treated as a perturbation on a background equilibrium.

We limit our consideration to an axially symmetric configura-tion for the magnetic-field configuration. The poloidal and toroidal components of the magnetic field are expressed by two functions Ψ and S, respectively, as follows:

$$\boldsymbol{B} = \boldsymbol{\nabla} \times \left(\frac{\Psi}{\varpi}\boldsymbol{e}_\phi\right) + \frac{S}{\varpi}\boldsymbol{e}_\phi, \tag{2}$$

where $\varpi = r\sin\theta$ is the cylindrical radius, and $\boldsymbol{e}_\phi$ is the azimuthal unit-vector in (r, θ, ϕ) coordinates. When the equilibrium is barotropic, i.e., the constant surfaces of ρ and P are parallel, the azimuthal current j_ϕ is described in the form

$$\frac{4\pi j_\phi}{c} = \rho\varpi\frac{dK}{d\Psi} + \frac{S}{\varpi}\frac{dS}{d\Psi}, \tag{3}$$

where the current function S should be a function of Ψ, and K is another function of Ψ. For the axially symmetric barotropic equilibrium, the acceleration due to the Lorentz force, which is abbreviated as $\boldsymbol{a} \equiv (c\rho)^{-1}\boldsymbol{j} \times \boldsymbol{B}$, is given by

$$\boldsymbol{a} = \frac{1}{4\pi}\boldsymbol{\nabla}K. \tag{4}$$

The force balance (1) is described by gradient terms of scalar functions.

The magnetic function Ψ is obtained by solving the Ampére–Biot–Savart law with the source term (Equation (3)) after the functional forms $S(\Psi)$ and $K(\Psi)$ are specified. For simplicity,

we assume that K is a linear function of Ψ, $K = K_0\Psi$, and $S = 0$ in Equation (3). The poloidal magnetic field is purely dipolar and is given by $\Psi = g(r)\sin^2\theta$. The radial function g is solved with appropriate boundary conditions: in a vacuum at the surface R, and $g = 0$ at the core-crust interface r_c. The latter refers to the magnetic field expelled from the core. For the case where the field penetrates into the core, g smoothly connects to the interior solution at r_c. We normalize the radial function by the dipole field strength B_0 at the surface, $g(R) = B_0R^2/2$.

The magnetic geometry discussed above is a simple initial model to examine the magnetic-field evolution. However, purely poloidal magnetic-field configurations are unstable according to an energy principle (Tayler 1973; Wright 1973; Markey & Tayler 1973) and numerical MHD simulation (Braithwaite & Nordlund 2006; Braithwaite 2009; Lander & Jones 2011a, 2011b; Mitchell et al. 2015). Dynamical simulations revealed that the final state after a few Alfvén-wave crossing times is a twisted-torus configuration, in which the poloidal and toroidal components of comparable field strengths are tangled. Moreover, recent 3D simulation shows a very asymmetric equilibrium (Becerra et al. 2022). These studies are concerned with the configuration in an entire star. The information relevant to our study corresponds to the magnetic field in a thin outer layer; therefore, the present understanding is quite incomplete. For example, the ratio of toroidal to poloidal components decreases near the surface, because the toroidal field should vanish outside the exterior. However, the ratio in the crust located near the surface is uncertain, almost zero or in the order of unity, although both components are comparable in magnitude inside the star. Initially, a simple magnetic-field configuration is used in this paper, but it is necessary to improve the configuration.

We discuss the nonbarotropic equilibrium of the magnetic field. From Equation (1), the acceleration owing to the Lorentz force satisfies

$$\boldsymbol{\nabla} \times \boldsymbol{a} = \boldsymbol{\nabla} \times \left(\frac{1}{\rho}\boldsymbol{\nabla}P\right) \neq 0. \tag{5}$$

The acceleration $\boldsymbol{a}$ is no longer described by the gradient of a scalar, but may be generalized as

$$\boldsymbol{a} = \frac{1}{4\pi}\boldsymbol{\nabla}K + \alpha\boldsymbol{\nabla}\beta, \tag{6}$$

where α and β are functions of r and θ, and $\boldsymbol{\nabla} \times \boldsymbol{a} = \boldsymbol{\nabla}\alpha \times \boldsymbol{\nabla}\beta \neq 0$ is assumed. Owing to almost arbitrary functions α and β, the constraint on the electric current, and hence to the magnetic-field configuration, is relaxed in the nonbarotropic case. Nonbarotropicity has been studied in magnetic deforma-tion (Mastrano et al. 2011, 2013, 2015). The barotropic (Haskell et al. 2008; Kojima et al. 2021b) and nonbarotropic models are significantly different (Mastrano et al. 2011, 2013, 2015) up to approximately one order of magnitude in the resulting ellipticity. The effect is important; however, the treatment remains unclear. Therefore, we introduce the models of $\boldsymbol{\nabla} \times \boldsymbol{a}$ to study nonbarotropicity in Section 4.

2.2. Magnetic-field Evolution

Our consideration is limited to the inner crust of a neutron star, where the mass density ranges from $\rho_c = 1.4 \times 10^{14}$ g cm^{-3} at the core–crust boundary r_c to the neutron-drip density $\rho_1 = 4 \times 10^{11}$ g cm^{-3} at $R = 12$ km. We ignore the outer crust

compared to *ocean* and treat the exterior region of $r > R$ as the vacuum. The crust thickness $\Delta r \equiv R - r_c$ is assumed to be $\Delta r/R = 0.05$, $\Delta r = 0.6$ km.

The Lorentz force $\boldsymbol{j} \times \boldsymbol{B}$ due to the magnetic-field evolution is not fixed in a secular timescale. The evolution in the crust is governed by the induction equation

$$\frac{\partial}{\partial t}\boldsymbol{B} = -\boldsymbol{\nabla} \times \left[\frac{1}{en_e}\boldsymbol{j} \times \boldsymbol{B} + \frac{c}{\sigma}\boldsymbol{j}\right], \tag{7}$$

where n_e is the electron-number density, and σ is the electric conductivity. The first term in Equation (7) represents the Hall drift, and the Hall timescale τ_H is estimated as follows:

$$\tau_H = \frac{4\pi en_{e\,c}(\Delta r)^2}{cB_0} = 7.9 \times 10^5 \text{ yr}\left(\frac{B_0}{10^{14}\text{G}}\right)^{-1}, \tag{8}$$

where the electron-number density n_{ec} at the core–crust boundary, crust thickness Δr, and dipole field strength B_0 at the surface are used. This timescale is shorter than that of the ohmic decay, which is the second term in Equation (7) in the strong-magnetic-field regime.

The Hall-ohmic evolution was numerically simulated in the Hall timescale (Pons & Geppert 2007; Kojima & Kisaka 2012; Viganò et al. 2013; Gourgouliatos et al. 2013; Gourgouliatos & Cumming 2014; Viganò et al. 2021) for axially symmetric models. Recently, the calculation has been extended to 3D models (Wood & Hollerbach 2015; Viganò et al. 2019; De Grandis et al. 2020; Gourgouliatos et al. 2020; Igoshev et al. 2021), revealing some of the effects ignored in the 2D models. Here, our calculation is limited to the early phase of the evolution in a simpler axial-symmetric model. We consider only the Hall drift term in Equation (7) and rewrite the equation as follows:

$$\frac{\partial}{\partial t}\boldsymbol{B} = -\boldsymbol{\nabla} \times \left[\frac{1}{en_e}\boldsymbol{j} \times \boldsymbol{B}\right] = -\boldsymbol{\nabla}\chi \times \boldsymbol{a} - \chi\boldsymbol{\nabla} \times \boldsymbol{a}, \tag{9}$$

where

$$\chi \equiv \frac{c\rho}{en_e} = \frac{4\pi\rho_c(\Delta r)^2}{\tau_H B_0}\hat{\chi}. \tag{10}$$

In Equation (10), $\hat{\chi}$ is a dimensionless function, which represents an inverse of the electron fraction. The electron-number density is obtained from the proton fraction of the equilibrium nucleus in *cold catalyzed matter*, i.e., it is determined in the ground state at $T = 0$ K. The data given by Douchin & Haensel (2001) is approximately fitted by a smooth function:

$$\hat{\chi} = \frac{\hat{\rho}^{1/2}}{0.32 + 0.66\hat{\rho}}, \tag{11}$$

where $\hat{\rho} \equiv \rho/\rho_c$. The spatial-density profile of a neutron star in $r_c \leqslant r \leqslant R$ is approximated as follows (Lander & Gourgouliatos 2019):

$$\hat{\rho} = \frac{\rho}{\rho_c} = \left[1 - \left(1 - \left(\frac{\rho_1}{\rho_c}\right)^{1/2}\right)\left(\frac{r - r_c}{\Delta r}\right)\right]^2. \tag{12}$$

The radial derivative $d\hat{\chi}/dr = (d\hat{\chi}/d\rho)(d\rho/dr)$ sharply changes, owing to an abrupt decrease in the density near the surface; however, $\hat{\chi}$ is a smoothly varying function of $\mathcal{O}(1)$. This functional behavior, which originates from the stellar-

density profile that is inherent in neutron stars, is crucial in our numerical calculation. Different fitting formulae are discussed for the different equation of state in Pearson et al. (2018); however, the difference in $\hat{\chi}$ is not significant in our analysis.

We consider the early phase of the evolution in the axially symmetric equilibrium model, in which $a_\phi = 0$. From Equation (9) at $t = 0$, we obtain that $\partial B_\phi/\partial t \neq 0$, but $\partial B_r/\partial t = \partial B_\theta/\partial t = 0$. The azimuthal component B_ϕ changes linearly with time t, whereas the poloidal components change with t^2. We limit our consideration to the lowest order of t only and ignore the change in the poloidal magnetic field. The early phase of the toroidal magnetic field may be approximated as

$$\delta B_\phi = \frac{\delta S}{\varpi}\left(\frac{t}{\tau_H}\right), \tag{13}$$

where δS is a function of r and θ. Because it is associated with δB_ϕ, the poloidal current changes; thus, the Lorentz force $\delta f = c^{-1}(\delta\boldsymbol{j} \times \boldsymbol{B} + \boldsymbol{j} \times \delta\boldsymbol{B})$ also changes. We observe that the nonzero component δf_ϕ because $\boldsymbol{j}_p = B_\phi = 0$ at $t = 0$, and we explicitly write

$$\delta f_\phi = \frac{1}{4\pi\varpi^2}[\boldsymbol{\nabla}\delta S \times \boldsymbol{\nabla}\Psi]_\phi\left(\frac{t}{\tau_H}\right). \tag{14}$$

2.3. Quasi-stationary Elastic Response

We assume that the solid crust elastically acts against the force δf_ϕ. The change is so slow that the elastic evolution is quasi-stationary. The acceleration $\partial^2\xi_i/\partial t^2$ of the elastic displacement vector ξ_i is dismissed; thus, the elastic force is balanced with the change in the Lorentz force, i.e., when the gravity and pressure in Equation (1) are assumed to be fixed. The elastic force is expressed by the trace-free strain tensor σ_{ij} and a shear modulus μ; therefore, the force balance is

$$\nabla_i(2\mu\sigma_\phi^i) + \delta f_\phi = 0, \tag{15}$$

$$\sigma_{ij} = \frac{1}{2}(\nabla_i\xi_j + \nabla_j\xi_i), \tag{16}$$

where incompressible motion $\nabla_k\xi^k = 0$ is assumed. Alternatively, the equivalent form is

$$\nabla_i\left[2\mu\sigma^{i\phi} + \frac{1}{4\pi}B^i\delta B^\phi\right] = 0. \tag{17}$$

The relevant component induced by δf_ϕ is the azimuthal displacement ξ_ϕ only, and the shear tensors that are determined by it are

$$\sigma_{r\phi} = \frac{r}{2}\left(\frac{\xi_\phi}{r}\right)_{,r}, \quad \sigma_{\theta\phi} = \frac{\sin\theta}{2r}\left(\frac{\xi_\phi}{\sin\theta}\right)_{,\theta}. \tag{18}$$

The shear modulus μ increases with density, and it may be approximated as a linear function of ρ, which is overall fitted to the results of a detailed calculation reported in a previous study (see Figure 43 in Chamel & Haensel 2008).

$$\mu = \frac{\mu_c\rho}{\rho_c}, \tag{19}$$

where $\mu_c = 10^{30}$ erg cm^{-3} at the core–crust interface. The shear speed v_s in Equation (19) is constant through the crust:

$$v_s = \left(\frac{\mu}{\rho}\right)^{1/2} = 8.5 \times 10^7 \text{cm s}^{-1}. \tag{20}$$

To solve Equation (15), we use an expansion method with the Legendre polynomials $P_l(\cos\theta)$ and radial functions $k_l(r)$, $a_l(r)$ as follows:

$$\xi_\phi = -\sum_{l\geqslant 1} r k_l P_{l,\theta}\left(\frac{t}{\tau_H}\right), \tag{21}$$

$$\delta f_\phi = -\sum_{l\geqslant 1} r^{-3} a_l P_{l,\theta}\left(\frac{t}{\tau_H}\right). \tag{22}$$

The displacement ξ_ϕ is decoupled with respect to the index l, owing to spherical symmetry, i.e., $\mu(r)$. Equation (15) is reduced to a set of ordinary differential equations for k_l (Kojima et al. 2022):

$$(\mu r^4 k_l')' - (l-1)(l+2)\mu r^2 k_l = -a_l, \tag{23}$$

where a prime $'$ denotes a derivative with respect to r. The boundary conditions for the radial functions k_l are given by the force balance across the surfaces at r_c and R. That is, the shear–stress tensor $\sigma_{r\phi}$ vanishes because other stresses for the fluid and magnetic field are assumed to be continuous. Explicitly, we have $k_l' = 0$ both at r_c and R. Note that a mode with $l=1$ is special in Equation (23), and k_1 is simply obtained by integrating a_1 with respect to r.

3. Elastic Deformation in Barotropic Model

The magnetic-field evolution in Equation (9) is driven by two terms, which are separately examined. We first consider the barotropic case, in which $\nabla \times \boldsymbol{a} = 0$. The evolution is driven by the first term in Equation (9), i.e., the distribution of the electron fraction. The linear growth term δS in Equation (13) is obtained using Equation (4) as

$$\delta S = \frac{2K_0 \rho_c (\Delta r)^2}{3B_0} \hat{\chi}' g \sin\theta P_{2,\theta}. \tag{24}$$

In the case where the poloidal magnetic field ($\Psi = g\sin^2\theta$) is confined in the crust, the constant K_0 is numerically obtained as $K_0 = 6.0 \times B_0/(\rho_c(\Delta r)^2)$. Alternatively, we express $K_0 = 8.6 \times 10^1 v_a^2/(B_0 R^2)$, where v_a is the Alfvén speed in terms of B_0 and ρ_1:

$$v_a = \frac{B_0}{\sqrt{4\pi\rho_1}} = 4.5 \times 10^7 \left(\frac{B_0}{10^{14}\text{G}}\right)\text{cm s}^{-1}. \tag{25}$$

The Lorentz force δf_ϕ in Equation (14) is calculated using Equation (24). For later convenience, we consider a general form $\delta S = y_l(r)\sin\theta P_{l,\theta}$. By using an identity for the Legendre polynomials, we reduce Equation (14) to

$$\delta f_\phi = \frac{1}{4\pi r^3}\left[(lg'y_l + 2gy_l')\frac{l+1}{2l+1}P_{l-1,\theta}\right.$$
$$\left. + (-(l+1)g'y_l + 2gy_l')\frac{l}{2l+1}P_{l+1,\theta}\right]\left(\frac{t}{\tau_H}\right). \tag{26}$$

Thus, the radial functions a_{l-1} and a_{l+1} in Equation (22) are induced by y_l. By numerically solving Equation (23) for k_l's, we obtain ξ_ϕ in Equation (21) and the shear–stress tensors, $\sigma_{r\phi}$ and $\sigma_{\theta\phi}$, in Equation (18). For Equation (24), the results are expressed using a combination of k_1 and k_3.

3.1. Results

The shear stress increases homologously with time, i.e., the spatial profile of the shear force is unchanged, but the magnitude increases with time. The numerical calculation provides the maximum shear stress σ_{max} with respect to (r, θ) in the crust as follows:

$$\sigma_{max} = 6.5 \times 10^1 \left(\frac{v_a}{v_s}\right)^2 \left(\frac{t}{\tau_H}\right). \tag{27}$$

The maximum is determined using a ratio of the shear speed v_s in Equation (20) to the Alfvén speed v_a in Equation (25). Elastic equilibrium is possible, only when the shear strain satisfies a particular criterion. We adopt the following (the Mises criterion) to determine the elastic limit:

$$\frac{1}{2}\sigma_{ij}\sigma^{ij} \leqslant (\sigma_{max})^2 \leqslant (\sigma_c)^2, \tag{28}$$

where σ_c is a number $\sigma_c \approx 10^{-2}$–10^{-1} (Horowitz & Kadau 2009; Baiko & Chugunov 2018; Caplan et al. 2018).

Thus, the period of the elastic response is limited by the constraint σ_c:

$$t \leqslant t_* \equiv 1.5 \times 10^{-3} \left(\frac{\sigma_c}{0.1}\right)\left(\frac{v_s}{v_a}\right)^2 \tau_H, \tag{29}$$

$$= 4.3 \times 10^3 \left(\frac{\sigma_c}{0.1}\right)\left(\frac{B_0}{10^{14}\text{G}}\right)^{-3}\text{yr}. \tag{30}$$

The breakup time t_* becomes short, i.e., a few years for magnetars with $B_0 = 10^{15}$ G. This is in agreement with the recurrent time of the activity in magnetars. However, the timescale exceeds 1 Myr for most neutron stars with $B < 10^{13}$G. Moreover, other evolution effects are important, and the present results are not applicable.

3.2. Energy

The stored elastic energy is obtained by numerically integrating over the entire crust:

$$\Delta E_{ela} = 2\pi \int_{r_c}^{R} r^2 dr \int_0^\pi \sin\theta d\theta \, \mu \sigma_{ij}\sigma^{ij}$$
$$= 5.8 \times 10^{-7} \mu_c R^3 \left(\frac{\sigma_c}{0.1}\right)^2 \left(\frac{t}{t_*}\right)^2, \tag{31}$$

where we have used R^3 instead of $R^2 \Delta r$ to normalize the crustal volume because $\Delta r/R = 0.05$ is fixed. The elastic energy E_{ela} increases up to $\approx 10^{41}$ erg at the breakup time t_*.

The magnetic energy ΔE_{mag} is also obtained by

$$\Delta E_{mag} = 2\pi \int_{r_c}^{R} r^2 dr \int_0^\pi \sin\theta d\theta \, \frac{(\delta B_\phi)^2}{8\pi}$$
$$= 2.0 \times 10^{-4} B_0^2 R^3 \left(\frac{\sigma_c}{0.1}\right)^2 \left(\frac{v_s}{v_a}\right)^4 \left(\frac{t}{t_*}\right)^2. \tag{32}$$
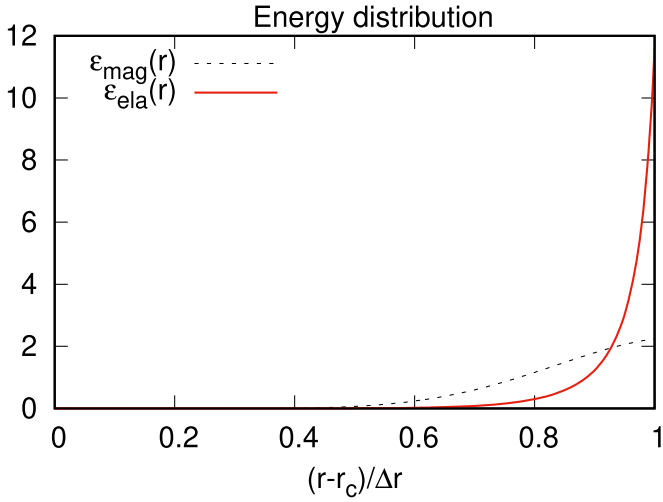
Figure 1. Energy distribution in crust as a function of the radius. Normalized energy density $\varepsilon(r)$ is plotted for magnetic energy, which is denoted by a dotted curve, and elastic energy, denoted by a solid curve.

Here, the shear speed appears in ΔE_{mag} because the breakup time t_* in Equation (29) is used instead of τ_H. The magnetic energy ΔE_{mag} at t_* is $\Delta E_{mag} \approx 2 \times 10^{43}(B_0/10^{14}\text{G})^{-2}$ erg. However, it is considerably smaller than the poloidal magnetic energy $E_{mag,p}$, which is numerically calculated as $E_{mag,p} = 3.8B_0^2 R^3 \approx 4 \times 10^{46}(B_0/10^{14}\text{G})^2$ erg. Note that total magnetic energy is conserved by the Hall evolution. Therefore, the same amount of polar magnetic energy decreases. However, we ignored the change in the poloidal component and its energy, which are proportional to t^2.

The ratio of Equations (31) and (32) is

$$\frac{d\Delta E_{ela}/dt}{d\Delta E_{mag}/dt} = \frac{\Delta E_{ela}}{\Delta E_{mag}} = 8.1 \times 10^{-2}\left(\frac{v_a}{v_s}\right)^2$$
$$= 2.3 \times 10^{-2}\left(\frac{B_0}{10^{14}\text{G}}\right)^2, \qquad (33)$$

where μ_c and B_0^2 are eliminated using v_s and v_a. The ratio is proportional to B_0^2; thus, ΔE_{mag} decreases in more strongly magnetized neutron stars. From the viewpoint of the energy flow from the poloidal component, the breakup energy $\Delta E_{ela} \approx 10^{41}$ at the terminal is fixed, but the ΔE_{mag} stored in the middle depends on the Hall drift speed. The elastic energy is efficiently accumulated through toroidal magnetic energy with an increase in B_0; $\Delta E_{ela} > \Delta E_{mag}$ for $B_0 > 6.7 \times 10^{14}$ G.

3.3. Spatial Distribution

Figure 1 shows spatial-energy densities $\varepsilon_{ela}(r)$ and $\varepsilon_{mag}(r)$, with regard to ΔE_{ela} and ΔE_{mag} in the crust, respectively. They are normalized as $\int \varepsilon_{ela}dr = \int \varepsilon_{ela}dr = 1$. Evidently, both energies are highly concentrated near the surface $r \approx R$. This property comes from the radial derivative of $\hat{\chi}$ in Equation (10). $d\hat{\chi}/dr = (d\hat{\chi}/d\rho)(d\rho/dr)$ is steep there even though $\hat{\chi}$ is $\mathcal{O}(1)$. The large value comes from $|d\rho/dr|$, i.e., a sharp decrease in density near the stellar surface, and it results in a smaller evolution timescale $\ll \tau_H$ in Equation (29).

Shear stresses $\sigma_{\theta\phi}$ and $\sigma_{r\phi}$ are induced by the axial displacement ξ_ϕ. A numerical calculation shows that the component $\sigma_{r\phi}$ is considerably larger than $\sigma_{\theta\phi}$; $(\sigma_{r\phi})_{max} \sim 200(\sigma_{\theta\phi})_{max}$. Figure 2
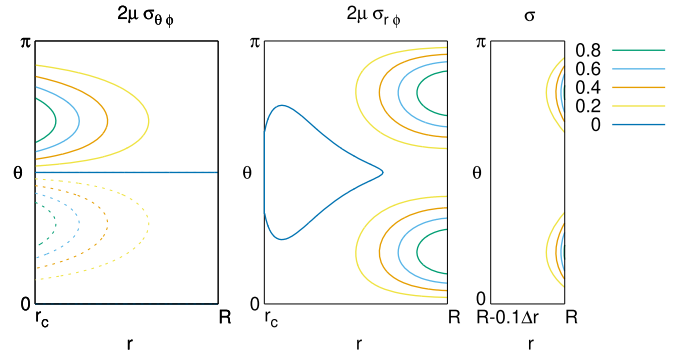

Figure 2. Contour map of stress tensor in crust. The left panel shows $2\mu\sigma_{\theta\phi}$, the middle $2\mu\sigma_{r\phi}$, and the right the magnitude σ. They are normalized according to the maximum. Negative values are plotted using a dotted curve in the left panel. The magnitude σ in the right panel is shown in the outer small region near the surface, $R - 0.1\Delta r \leqslant r \leqslant R$.

shows their spatial distribution using a contour map of $2\mu\sigma_{\theta\phi}$ and $2\mu\sigma_{r\phi}$ in the $r-\theta$ plain. The angular dependence of $\sigma_{\theta\phi}$ is $\sigma_{\theta\phi} \propto \sin^2\theta\cos\theta$, and it is antisymmetric with respect to the equator ($\theta = \pi/2$). Moreover, $\sigma_{r\phi}$ is the sum of $P_{1,\theta}$ and $P_{3,\theta}$, and it is symmetric with respect to $\theta = \pi/2$. The magnitude $\sigma = (\sigma_{ij}\sigma^{ij}/2)^{1/2}$ is also shown in the right panel, and σ is sharp near the surface, as expected from the sharp energy-density distribution in Figure 1.

We discuss the modification of the poloidal magnetic field at the core–crust boundary. Thus far, the magnetic field is expelled there. When the field is penetrated to the core, the function g near the boundary and the constant K_0 in Equation (24) are changed. The former is unimportant because the function $\hat{\chi}'$ is sharp near the surface, and this fact determines the result, as shown in Figures 1 and 2. The constant K_0 for the penetrated field is 4.1×10^{-2} times smaller than that for the expelled one. Consequently, the profile is almost unchanged, but the break time t_* increases by a factor of 24 with the same dipole field strength.

4. Elastic Deformation in Nonbarotropic Model

We consider the evolution driven by the second term, $\nabla \times \boldsymbol{a} \neq 0$ in Equation (9), which originates from the nonbarotropic material distribution. However, $\nabla \times \boldsymbol{a}$ and the corresponding magnetic field cannot be easily estimated, unless the nonbarotropic property is specified. A large freedom of choice hinders our analysis. Therefore, we simply model the term $\nabla \times \boldsymbol{a}$ and understand the nonbarotropic effect in its magnitude and property. For this purpose, we assume $a_\phi = 0$, and

$$(\nabla \times \boldsymbol{a})_\phi = \frac{N^2}{(\Delta r)^2}F_n(r)P_{2,\theta}, \qquad (34)$$

where N is a constant that characterizes the nonbarotropic strength, and it has the dimension of velocity. Additionally, F_n is a nondimensional radial function. We consider a small deviation from the barotropic case, for which the second term in Equation (6) is smaller than the first term. Therefore, the magnetic field is approximated using the barotropic case, i.e., the poloidal magnetic function Ψ and $S = 0$. This treatment constrains the normalization N in Equation (34) with respect to the magnitude. By the dimensional argument, we have $|N| \ll R/t_{ff} \sim 10^9$ cm s^{-1}, where t_{ff} is a freefall timescale.

Table 1
Numerical Values in Equations (36), (37), and (38)

Model	n_1 (t_*)	n_2 (ΔE_{ela})	n_3 (ΔE_{mag})
In	8.0×10^{-3}	2.1×10^{-3}	7.2×10^{-7}
Out	1.2×10^{-2}	2.4×10^{-4}	1.0×10^{-6}
Average	3.6×10^{-3}	2.9×10^{-4}	2.9×10^{-7}
Min	1.9×10^{-3}	0.49×10^{-4}	0.73×10^{-7}
Max	5.5×10^{-3}	7.0×10^{-4}	6.4×10^{-7}

Moreover, $|N| < v_a$ and $|N| < v_s \sim 10^8 \, \text{cm s}^{-1}$ are also likely because the crust is in magneto-elastic equilibrium.

The angular dependence of Equation (34) is chosen for δS to be the same as in Equation (24). The radial function F_n has a maximum that is normalized as unity, and it vanishes at inner and outer boundaries; the function is modeled as follows:

$$F_n = \frac{256}{27} \left(\frac{r - r_c}{\Delta r} \right)^n \left(\frac{R - r}{\Delta r} \right)^{4-n}, \quad (35)$$

where $n = 1$ or 3. The model with $n = 1$ is referred to as the *in* model because the maximum is located at $r = r_c + \Delta r/4$, whereas that with $n = 3$ is referred to as the *out* model because the maximum is located at $r = R - \Delta r/4$.

4.1. Results of a Simple Model

We neglect the first term in Equation (9), and consider the magnetic-field evolution driven by the term $\nabla \times \boldsymbol{a}$ (Equation (34)) only. Similar to the calculations in Section 3, a linearly growing shear–stress is obtained, owing to ξ_ϕ. The period of the elastic response is limited by

$$t \leqslant t_* \equiv n_1 \times \left(\frac{\sigma_c}{0.1} \right) \left(\frac{v_s}{N} \right)^2 \tau_H, \quad (36)$$

where n_1 is a number of the order of 10^{-2}, depending on the models, as listed in Table 1. Owing to our simple modeling, the comparison between the barotropic and nonbarotropic models is uncomplicated; the Alfvén speed v_a in Equation (29) is formally substituted by N in Equation (36).

The elastic energy ΔE_{ela} and toroidal magnetic energy ΔE_{mag} stored inside the crust are also summarized as follows:

$$\Delta E_{ela} = n_2 \times \mu_c R^3 \left(\frac{\sigma_c}{0.1} \right)^2 \left(\frac{t}{t_*} \right)^2, \quad (37)$$

$$\Delta E_{mag} = n_3 \times B_0^2 R^3 \left(\frac{\sigma_c}{0.1} \right)^2 \left(\frac{v_s}{N} \right)^4 \left(\frac{t}{t_*} \right)^2, \quad (38)$$

where $n_2 \approx 6 \times 10^{-4}$, and $n_3 \approx 10^{-6}$, as listed in Table 1. The elastic energy ΔE_{ela} does not depend on N; however, the timescale for Equation (36) does. The amount of elastic energy is unrelated to the detailed process, which affects the accumulation speed in the crust. At the breakup time, the elastic energy is $\Delta E_{ela} = 2 \times 10^{44} - 2 \times 10^{45}$ erg. This energy is more than three orders of magnitude larger than the energy from Equation (31) considered in the previous section. The difference is made clear when considering the energy–density distribution.

Figure 3 shows the energy–density distribution in the crust. The difference in the toroidal magnetic energy clearly originates in the model choice; the energy density spreads
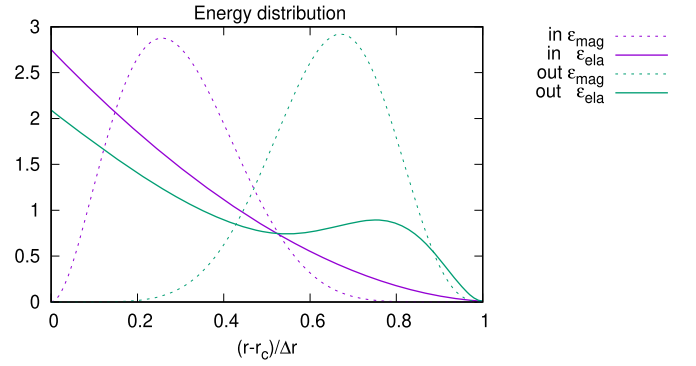

Figure 3. Spatial distribution of magnetic energy (dotted curve) and elastic energy (solid curve) in the crust. Normalized energy densities $\varepsilon(r)$ are plotted for two models.
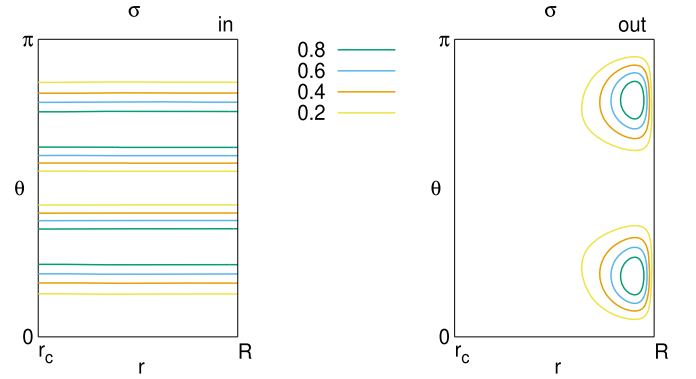

Figure 4. Crust contour map of magnitude of stress tensor normalized using the maximum. The left panel for the *in* model shows $\sigma \approx \sigma_{\theta\phi}$, whereas the right panel for the *out* model shows $\sigma \approx \sigma_{r\phi}$.

more toward the interior for the *in* model, whereas it spreads more toward the exterior for the *out* model. Most of the elastic energy is localized near the inner core–crust boundary; however, the distribution in the *out* model is shifted outwardly with the second peak ($\sim r_c + 0.8\Delta r$) produced by the input model. The integrated elastic energy in the *out* model becomes one order of magnitude smaller than that in the *in* model.

The amount of elastic energy at the breakup clearly depends on the spatial distribution of the energy density because the shear modulus μ is a strongly decreasing function toward the surface. The elastic limit of the entire crust is typically determined using a condition to the shear σ_{ij} near the surface. The total elastic energy $\sim \int \mu \sigma_{ij} \sigma^{ij} d^3 x$ thereby decreases as $\sigma_{ij} \sigma^{ij}$ is localized toward the exterior. The breakup elastic energy $\Delta E_{ela} \sim 10^{41}$ erg at t_* in the previous section is an extreme case because the energy density is concentrated near the surface.

Figure 4 shows the magnitude of shear stress σ inside the crust. The contours of σ in the two models are different. We identified that the dominant component in the *in* model (left panel) is $\sigma_{\theta\phi}$, which has an angular dependence that is described by $\sigma_{\theta\phi} \propto \sin^2 \theta \cos \theta$. The maximum of σ is given along a line $\cos \theta = \pm 1/\sqrt{3}$ ($\theta \sim 55°$, $125°$). The component $\sigma_{r\phi}$ is dominant in the *out* model (right panel). Sharp peaks are localized near the surface, similar to the right panel in Figure 2; however, the localization is not as pronounced as in Figure 2. The magnitude σ, which is important to determine the critical limit, is large near the surface.
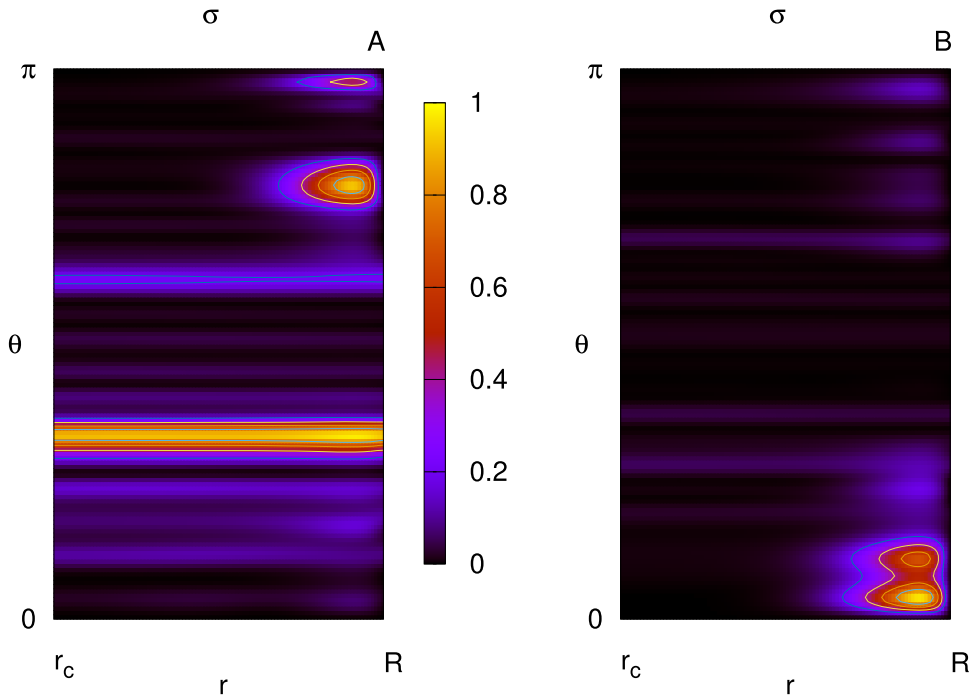
Figure 5. Color contour map of crust for the magnitude of the stress tensor σ normalized using the maximum; two models are compared.

4.2. Results of a Model Including Higher Multipoles

In a more realistic situation, the solenoidal acceleration may fluctuate spatially. We consider the sum of multipole components $P_{l,\theta}$:

$$(\nabla \times a)_\phi = \frac{N^2}{(\Delta r)^2} \sum_{l=2}^{l_{max}} \left(\frac{l}{2}\right)^{-4/3} \lambda_l F_n(r) P_{l,\theta}, \quad (39)$$

where $\lambda_l F_n$ is a radial function that is randomly selected from $\pm F_1$ or $\pm F_3$ depending on l. As discussed for Equation (26), the radial function k_l in the azimuthal displacement ξ_ϕ is solved for the source term that originates from $\lambda_{l-1}F_n$ and $\lambda_{l+1}F_n$; thus, the amplitude $|k_l|$ fluctuates according to the randomness. We fix the overall constant N. Equation (39) is reduced to Equation (34) when $l_{max} = 2$. Moreover, higher l-modes, up to $l_{max} = 30$ with the power-law weight, are included. The power-law index is considerably steep; therefore, the dominant component is still described by $l = 2$.

We calculated 20 models by randomly mixing $\lambda_l F_n$. The numerical results are summarized in the same forms as Equations (36)–(38), and the numerical values n_i ($i = 1, 2, 3$) in the breakup time and energies are listed in Table 1 according to the average, minimum, and maximum for the 20 models. These numerical values are of the same order as those by a single mode with $l = 2$ because we include higher l-modes as the correction. Interestingly, the breakup time t_* generally becomes shorter than that for a single mode with $l = 2$ because the higher modes $l > 3$ are cooperative.

Figure 5 demonstrates the spatial distribution of the shear–stress tensor. Two models are shown using contours of the magnitude of σ. In the left panel, the subcritical regions are on a constant θ line with a sharp peak near the surface. In the other model (right panel), a peak is observed at $\theta = 0$ near the surface. The angular position of the peak is different between the two models. As shown in Figure 4, the spatial pattern along a constant θ comes from the component $\sigma_{\theta\phi}$, whereas the sharp peak near the surface is due to $\sigma_{r\phi}$. The mixing of the two types of radial functions, F_1 and F_3, and angular functions P_l with random phases and weights, only complicates the spatial distribution of σ. A sharp peak is likely to be located near the surface. The outer part of the crust is always fragile; thus, the breakup time becomes shorter.

5. Summary and Discussion

We have considered the evolution of elastic deformation over a secular timescale (>1 yr) starting from zero displacement. The initial state is related to the dynamic force balance that is determined within a second. When a neutron star cools below the melting temperature $T \sim 10^9$ K, its crust is crystallized. Meanwhile, the pressure, gravity, and Lorentz force are balanced without the elastic force. In another situation, the elastic energy settles to the ground state, and zero displacement occurs after the energy is completely released at the crustal fracture. Therefore, the initial condition is simple and natural.

When the MHD equilibrium is axisymmetric, the azimuthal component of the magnetic field increases linearly according to the Hall evolution. Consequently, the elastic deformation in the azimuthal direction is induced to cancel the change in the Lorentz force, and the shear strain gradually increases. We estimate the range of the elastic response. Beyond the critical limit, the crust responds plastically or fractures. Our calculations provide the breakup time and shear distribution at the threshold.

For the barotropic case, the breakup time until the fracture is proportional to the cube of the magnetic-field strength. The time becomes a few years for a magnetar with a surface dipole of $B_0 \sim 10^{15}$ G, when the field is located outside the core. However, it exceeds 1 Myr for most radio pulsars ($B_0 < 10^{13}$G), and the process is irrelevant to them. In addition to the field strength, the timescale is typically shortened by a factor of 10^{-3} smaller than the Hall timescale because the elastic displacement is highly concentrated near the surface. The driven mechanism is related

to the instability associated with electron-density gradients (Wood et al. 2014). The distribution in any realistic model of neutron-star crusts is considerably sharp; therefore, the evolution is general. Another type of Hall-drift instability occurs in the presence of a nonuniform magnetic field (Rheinhardt & Geppert 2002), which is not considered here, and its energy would be smaller, owing to the size of the irregularity. In our calculation, we do not follow the instability; instead, we estimate the energy transferred to the elastic deformation.

The elastic energy at the critical limit in the model driven by the electron-number-density gradient is $\sim 10^{41}$ erg. The amount of energy is of the same order as that of short bursts in magnetars. The breaktime of ~ 10 yr also reconciles with the observed recurrent time of the bursts. However, the energy $\sim 10^{41}$ erg is smaller than that of giant flares $\sim 10^{44}$–10^{46} erg (Turolla et al. 2015; Kaspi & Beloborodov 2017; Esposito et al. 2021, for a review). The total elastic energy derived in Section 3 is based on the electron-number density in cold catalyzed matter, i.e., the ground state at $T = 0$ K. If the assumption was relaxed, the nonbarotropic effects might increase the total elastic energy, as considered in Section 4.

When the pressure distribution is no longer expressed solely by the density ρ, the magnetic evolution is affected by the solenoidal acceleration $\boldsymbol{a} = \boldsymbol{\nabla} \times (\rho^{-1} \boldsymbol{\nabla} P) \neq 0$. We have also considered this effect by creating the model in terms of a spatial function and an overall strength parameter, which are assumed to be constant in time in our nonbarotropic model. Using the simplified model, we calculated the breakup time of the crustal failure and the energies stored in the crust. The results were comparable to those for the barotropic case. The strength parameter significantly affects the breakup time; the larger the magnitude, the shorter the breakup time. However, the amount of elastic energy at the breakup does not depend on the strength parameter, but only on the spatial function. The maximum elastic energy considerably increases up to $\sim 10^{45}$ erg. However, the model is still primitive, and thermal evolution should also be incorporated to investigate a more realistic situation.

The maximum energy has been explored thus far; however, a natural question arises. What is the fraction of energy that is released at the crustal fracture when the strain exceeds the threshold? This question is important, but at present unclear, owing to our lack of understanding of the fracture dynamics. Therefore, we present the following discussion. As depicted in Figure 5, in the realistic mixture model, a peak of shear strain σ is probably located near the surface, where the crust is fragile. Therefore, the fracture should not include the whole crust, but only the shallow crust. For this case, the released energy is not the whole elastic energy $\sim 10^{45}$ erg, but the energy stored in the restricted region, i.e., a small fraction of the total, probably $\sim 10^{41}$ erg.

The elastic deformation driven by the Hall evolution is simulated for the first time. The critical structure at the breakup time is crucial for subsequent evolution, irrespective of the plastic evolution or fracturing. The transition may appear as a burst on a magnetar. The magnetic-field rearrangement due to a mimic burst was incorporated in the Hall evolution (Pons & Perna 2011; Viganò et al. 2013; Dehman et al. 2020), without solving the elastic deformation. These studies estimated the critical state based on the magnetic stress $\mathcal{M}_{ij}$. In numerical simulations, $\mathcal{M}_{ij}$ changed, and the critical state was assumed when a condition among $\mathcal{M}_{ij}$ reached the threshold value. Similar approximations for the elastic limit, which were derived solely from $\mathcal{M}_{ij}$, were used in a previous study

(Lander et al. 2015; Lander & Gourgouliatos 2019; Suvorov & Kokkotas 2019). Mathematically, the shear stress σ_{ij} cannot be derived from $\mathcal{M}_{ij}$ without solving the appropriate differential equation $\nabla_j (2\mu \sigma_i^j + \mathcal{M}_i^j) = 0$ (see Equation (17)). Therefore, previous results with the criterion $\mathcal{M}_{ij}$ are questionable.

Our calculation shows that the period of elastic evolution is typically 10^{-3} times the Hall timescale; however, this value depends on the strength and geometry of the magnetic field. The timescale is shorter than the ohmic timescale for $B \geqslant 10^{13}$ G. The magnetic-field evolution beyond the period may be described by including the viscous bulk flow when the crust responds plastically. The effect of the plastic flow on the Hall–ohmic evolution was considered by assuming a plastic flow everywhere in the crust (Kojima & Suzuki 2020) or by using an approximated criterion (Lander & Gourgouliatos 2019; Gourgouliatos & Lander 2021; Gourgouliatos 2022). The effect may be regarded as additional energy lost to the ohmic decay. However, the post-failure evolution significantly depends on the modeling in the numerical simulation (Gourgouliatos & Lander 2021; Gourgouliatos 2022). That is, the region of plastic flow is either local or global when the failure criterion is satisfied. Therefore, the manner of incorporation of crust failure in the numerical simulation must be explored.

Finally, further investigation is required before the elastic deformation toward the crust failure can be considered a viable model. The effect of magnetic-field configuration should be considered because there are many degrees of freedom concerning it. Moreover, the outer boundary, i.e., inner–outer crust boundary or exterior magnetosphere is crucial as the crust becomes more fragile with increasing radius. Meanwhile, the electric conductivity decreases, and the ohmic loss becomes more important. By considering coupling to an exterior magnetosphere, twisting of the magnetosphere as well as crustal motion will be calculated in a secular timescale to match astrophysical observations, e.g., to describe the prestage of outbursts, like SGR 1830–0645 (Younes et al. 2022).

ORCID iDs

Yasufumi Kojima https://orcid.org/0000-0002-4402-3568

References

Abbott, R., Abe, H., Acernese, F., et al. 2021a, ApJ, 921, 80
Abbott, R., Abe, H., Acernese, F., et al. 2021b, ApJL, 913, L27
Abbott, R., Abe, H., Acernese, F., et al. 2022, PhRvD, 106, 042003
Alpar, M. A., Pines, D., Anderson, P. W., & Shaham, J. 1984, ApJ, 276, 325
Anderson, P. W., & Itoh, N. 1975, Natur, 256, 25
Baiko, D. A., & Chugunov, A. I. 2018, MNRAS, 480, 5511
Basu, A., Shaw, B., Antonopoulou, D., et al. 2022, MNRAS, 510, 4049
Becerra, L., Reisenegger, A., Valdivia, J. A., & Gusakov, M. E. 2022, MNRAS, 511, 732
Bochenek, C. D., Ravi, V., Belov, K. V., et al. 2020, Natur, 587, 59
Braithwaite, J. 2009, MNRAS, 397, 763
Braithwaite, J., & Nordlund, Å. 2006, A&A, 450, 1077
Caplan, M. E., Schneider, A. S., & Horowitz, C. J. 2018, PhRvL, 121, 132701
Chamel, N., & Haensel, P. 2008, LRR, 11, 10
CHIME/FRB Collaboration, Andersen, B. C., Bandura, K. M., et al. 2020, Natur, 587, 54
De Grandis, D., Turolla, R., Wood, T. S., et al. 2020, ApJ, 903, 40
Dehman, C., Viganò, D., Rea, N., et al. 2020, ApJL, 902, L32
Dib, R., Kaspi, V. M., & Gavriil, F. P. 2008, ApJ, 673, 1044
Douchin, F., & Haensel, P. 2001, A&A, 380, 151

Espinoza, C. M., Lyne, A. G., Stappers, B. W., & Kramer, M. 2011, MNRAS, 414, 1679
Esposito, P., Rea, N., & Israel, G. L. 2021, ASSL, 461, 97
Franco, L. M., Link, B., & Epstein, R. I. 2000, ApJ, 543, 987
Giliberti, E., Cambiotti, G., Antonelli, M., & Pizzochero, P. M. 2020, MNRAS, 491, 1064
Gittins, F., Andersson, N., & Jones, D. I. 2021, MNRAS, 500, 5570
Gourgouliatos, K. N. 2022, arXiv:2202.06662
Gourgouliatos, K. N., & Cumming, A. 2014, MNRAS, 438, 1618
Gourgouliatos, K. N., Cumming, A., Reisenegger, A., et al. 2013, MNRAS, 434, 2480
Gourgouliatos, K. N., Hollerbach, R., & Igoshev, A. P. 2020, MNRAS, 495, 1692
Gourgouliatos, K. N., & Lander, S. K. 2021, MNRAS, 506, 3578
Haskell, B., Jones, D. I., & Andersson, N. 2006, MNRAS, 373, 1423
Haskell, B., Samuelsson, L., Glampedakis, K., & Andersson, N. 2008, MNRAS, 385, 531
Horowitz, C. J., & Kadau, K. 2009, PhRvL, 102, 191102
Igoshev, A. P., Gourgouliatos, K. N., Hollerbach, R., & Wood, T. S. 2021, ApJ, 909, 101
Kaspi, V. M., & Beloborodov, A. M. 2017, ARA&A, 55, 261
Kojima, Y., & Kisaka, S. 2012, MNRAS, 421, 2722
Kojima, Y., Kisaka, S., & Fujisawa, K. 2021a, MNRAS, 506, 3936
Kojima, Y., Kisaka, S., & Fujisawa, K. 2021b, MNRAS, 502, 2097
Kojima, Y., Kisaka, S., & Fujisawa, K. 2022, MNRAS, 511, 480
Kojima, Y., & Suzuki, K. 2020, MNRAS, 494, 3790
Lander, S. K., Andersson, N., Antonopoulou, D., & Watts, A. L. 2015, MNRAS, 449, 2047
Lander, S. K., & Gourgouliatos, K. N. 2019, MNRAS, 486, 4130
Lander, S. K., & Jones, D. I. 2011a, MNRAS, 412, 1394
Lander, S. K., & Jones, D. I. 2011b, MNRAS, 412, 1730
Li, X., Ge, M., Lin, L., et al. 2022, ApJ, 931, 56
Markey, P., & Tayler, R. J. 1973, MNRAS, 163, 77
Mastrano, A., Lasky, P. D., & Melatos, A. 2013, MNRAS, 434, 1658
Mastrano, A., Melatos, A., Reisenegger, A., & Akgün, T. 2011, MNRAS, 417, 2288
Mastrano, A., Suvorov, A. G., & Melatos, A. 2015, MNRAS, 447, 3475
Mereghetti, S., Savchenko, V., Ferrigno, C., et al. 2020, ApJL, 898, L29
Mitchell, J. P., Braithwaite, J., Reisenegger, A., et al. 2015, MNRAS, 447, 1213
Payne, D. J. B., & Melatos, A. 2004, MNRAS, 351, 569
Pearson, J. M., Chamel, N., Potekhin, A. Y., et al. 2018, MNRAS, 481, 2994
Pons, J. A., & Geppert, U. 2007, A&A, 470, 303
Pons, J. A., & Perna, R. 2011, ApJ, 741, 123
Rencoret, J. A., Aguilera-Gómez, C., & Reisenegger, A. 2021, A&A, 654, A47
Rheinhardt, M., & Geppert, U. 2002, PhRvL, 88, 101103
Suvorov, A. G., & Kokkotas, K. D. 2019, MNRAS, 488, 5887
Tayler, R. J. 1973, MNRAS, 161, 365
Turolla, R., Zane, S., & Watts, A. L. 2015, RPPh, 78, 116901
Ushomirsky, G., Cutler, C., & Bildsten, L. 2000, MNRAS, 319, 902
Viganò, D., Garcia-Garcia, A., Pons, J. A., Dehman, C., & Graber, V. 2021, CoPhC, 265, 108001
Viganò, D., Rea, N., Pons, J. A., et al. 2013, MNRAS, 434, 123
Viganò, D., Martínez-Gómez, D., Pons, J. A., et al. 2019, CoPhC, 237, 168
Wadiasingh, Z., & Chirenti, C. 2020, ApJL, 903, L38
Wood, T. S., & Hollerbach, R. 2015, PhRvL, 114, 191101
Wood, T. S., Hollerbach, R., & Lyutikov, M. 2014, PhPl, 21, 052110
Wright, G. A. E. 1973, MNRAS, 162, 339
Younes, G., Lander, S. K., Baring, M. G., et al. 2022, ApJL, 924, L27